Monthly Notices of the ROYAL ASTRONOMICAL SOCIETY

MNRAS **469,** 4012–4021 (2017) doi:10.1093/mnras/stx1094
Advance Access publication 2017 May 8

Chemical enrichment of stars due to accretion from the ISM during the Galaxy's assembly

Sijing Shen,[1,2]★ Girish Kulkarni,[2]★ Piero Madau[3] and Lucio Mayer[4]

[1]*Institute of Theoretical Astrophysics, University of Oslo, Postboks 1029, 0315 Oslo, Norway*
[2]*Institute of Astronomy and Kavli Institute of Cosmology, University of Cambridge, Madingley Road, Cambridge CB3 0HA, UK*
[3]*Department of Astronomy and Astrophysics, University of California, 1156 High Street, Santa Cruz, CA 95064, USA*
[4]*Institute of Theoretical Physics, University of Zurich, Winterthurerstrasse 190, CH-9057 Zurich, Switzerland*

Accepted 2017 May 4. Received 2017 May 4; in original form 2016 December 8

ABSTRACT

Using the Eris zoom-in cosmological simulation of assembly of a Milky Way analogue, we study the chemical enrichment of stars due to accretion of metal-enriched gas from the interstellar medium (ISM) during the Galaxy's development. We consider metal-poor and old stars in the Galactic halo and bulge through the use of stellar orbits, gas density and metallicity distributions in Eris. Assuming spherically symmetric Bondi–Hoyle accretion, we find that halo and bulge stars accrete metals at the rate of about 10^{-24} and 10^{-22} $M_\odot$ yr^{-1}, respectively, at redshifts $z \lesssim 3$, but this accretion rate increases roughly a hundred-fold to about 10^{-20} $M_\odot$ yr^{-1} at higher redshifts due to increased gas density. Bulge and halo stars accrete similar amounts of metals at high redshifts when kinematically distinct bulge and halo have not yet developed, and both sets of stars encounter a similar metal distribution in the ISM. Accretion alone can enrich main-sequence stars up to [Fe/H] ~ -2 in extreme cases, with the median enrichment level due to accretion of about [Fe/H] ~ -6 to -5. Because accretion mostly takes place at high redshifts, it is α-enriched to [α/Fe] ~ 0.5. We find that accretive metal enrichment is sufficient to affect the predicted metallicity distribution function of halo stars at [Fe/H] < -5. This can hinder attempts to infer natal chemical environment of metal-poor stars from their observed enrichment. Peculiar enrichment patterns such as those predicted to arise from pair-instability supernovae could help in disentangling the natal and accreted metal content of stars.

Key words: accretion, accretion discs – stars: abundances – stars: chemically peculiar – stars: Population III – Galaxy: abundances – Galaxy: stellar content.

1 INTRODUCTION

Stars are thought to preserve a chemical record of their natal environment in their presently observed metal abundance (Frebel & Norris 2013). This makes old, low-mass, metal-poor stars in the Galaxy an important probe of star formation at the earliest cosmological times (Frebel & Norris 2015). Stars with masses less than 1 $M_\odot$ have lifetimes longer than 12.7 Gyr (Maeder & Meynet 1989). As a result, stars formed in this mass range at redshifts $z > 6$ can survive until the present day. These stars probe conditions during the formation of the Galaxy and can likely reveal properties of the earliest, metal-free, so-called Population III stars. Some of today's low-mass stars could themselves be Population III (Johnson 2015) as recent simulations of the formation of Population III stars have increasingly favoured the view that these stars could have had masses less than 1 $M_\odot$ (Clark et al. 2011; Greif et al. 2011; Dopcke et al. 2013; Hirano et al. 2014; Stacy & Bromm 2014; Susa, Hasegawa & Tominaga 2014; Machida & Nakamura 2015; Stacy, Bromm & Lee 2016).

In the last few decades, significant effort has been made to find metal-poor stars in the Galactic halo (Bond 1981; Beers, Preston & Shectman 1985; Ryan & Norris 1991; Beers, Preston & Shectman 1992; Carney et al. 1996; Christlieb 2003; Norris et al. 2007; Yanny et al. 2009; Caffau et al. 2011; Keller et al. 2014) as well as in the bulge (Casey & Schlaufman 2015; Howes et al. 2015; Jacobson et al. 2015; Howes et al. 2016; Ness & Freeman 2016). These surveys have revealed about 400 stars with iron abundance [Fe/H] < -3 and 8 stars with [Fe/H] < -7.5 to -4.5 (Frebel & Norris 2015), based on high-resolution spectroscopic observations of candidate extremely metal-poor stars. Abundances of a variety of other elements such as lithium, carbon, magnesium and calcium have also been measured in these stars. None of these stars has the minimum observable metal abundance, which is set by the capabilities of spectrographs

★E-mail: shens@astro.uio.no (SS); kulkarni@ast.cam.ac.uk (GK)

and currently corresponds to the metal abundance of a cool red giant with $T_{\rm eff} = 4500$ K and $\log g = 1.5$ with observed Ca II K line strength of 20 mÅ (Frebel & Norris 2015). Thus, no Population III star has yet been discovered.

Still, models of galaxy formation that account for metal production in stars and supernova-driven metal enrichment of the interstellar medium (ISM) can be used to infer constraints on early star formation, including Population III star formation, from the chemical properties of observed metal-poor stars (Barkana & Loeb 2001; Bromm & Larson 2004; Ciardi & Ferrara 2005; Glover 2005; Ripamonti & Abel 2006; Schneider et al. 2006; Salvadori, Schneider & Ferrara 2007; Bromm et al. 2009; Komiya et al. 2009, 2010; Schneider et al. 2012; Bromm 2013; Frebel & Norris 2013; de Bennassuti et al. 2014; Marassi et al. 2014; Hartwig et al. 2015; Smith et al. 2015; Griffen et al. 2016; Ishiyama et al. 2016; Stacy et al. 2016; de Bennassuti et al. 2017). For example, Salvadori et al. (2007) derived constraints on the typical mass of Population III stars $m_{\rm PopIII}$ and the critical gas metallicity $Z_{\rm cr}$ below which Population III stars can form. They argued that non-detection of a metal-free star constrains $Z_{\rm cr} > 0$ and $m_{\rm PopIII} > 0.9$ M$_\odot$. In their model, the observed metallicity distribution function (MDF) of metal-poor stars in the Galactic halo was well fit by $Z_{\rm cr} = 10^{-4}$ Z$_\odot$ and $m_{\rm PopIII} = 200$ M$_\odot$. Schneider et al. (2012) showed that the elemental abundance pattern of the metal-poor star SDSS J102915+172927, which has metallicity $Z = 4.5 \times 10^{-5}$ Z$_\odot$ and mass less than 0.8 M$_\odot$, can be accounted for by the chemical yields of core-collapse supernovae with metal-free progenitor stars having masses 20 and 35 M$_\odot$. By tracking the production of dust in these supernovae, Schneider et al. (2012) argued that the existence of SDSS J102915+172927 implied that dust cooling played an important role in the formation of the first low-mass Population II stars. Recently, Hartwig et al. (2015) argued that if no metal-free star is detected in a sample of 2×10^7 halo stars then $m_{\rm PopIII} > 0.8$ M$_\odot$ at 99 per cent confidence level.

However, all of the above attempts at exploiting the metal abundance properties of metal-poor stars assume that these stars preserve the metal abundance properties of their natal star-forming clouds. This assumption can break down if stars are able to efficiently accrete metals from the ISM as they orbit in the potential well of the Galaxy throughout their lifetime. Due to their large ages, low-mass metal-poor stars can potentially interact with a large column of ISM gas, depending on the stellar orbits. During this time, the ISM itself becomes increasingly enriched due to metal production from other stars, as evidenced by the existence of an age-metallicity relation in high-redshift galaxies (Erb et al. 2006; Maiolino et al. 2008; Rafelski et al. 2012). Accretion of metals from this enriched ISM can pollute old metal-poor stars, and can result in metal abundance patterns that can be quite different from the original metal abundance patterns of these stars. As a result, depending on the magnitude of this effect, errors can be introduced in any inference about high-redshift star formation drawn from the chemical properties of old metal-poor stars.

Chemical enrichment of stars due to accretion from the ISM has been studied over the last several decades (Talbot & Newman 1977; Alcock & Illarionov 1980; Yoshii 1981; Iben 1983; Frebel, Johnson & Bromm 2009; Komiya et al. 2009, 2010; Johnson & Khochfar 2011; Hattori et al. 2014; Johnson 2015; Komiya, Suda & Fujimoto 2015). Assuming that stars accrete only when they pass through the Galactic disc and assuming a static Galactic disc with height 100 pc and density $n \sim 5$ cm^{-3}, Frebel et al. (2009) calculated metal accretion for 474 stars using their kinematic measurements from the Sloan Digital Sky Survey, and concluded that accretion is generally negligible. Komiya et al. (2009, 2010, 2015) considered metal accretion of metal-poor stars in a semi-analytical galaxy formation model built on halo merger trees obtained using the extended Press–Schechter formalism and concluded that Population III survivors can be enriched up to [Fe/H] ~ -5 due to accretion from the ISM. Johnson & Khochfar (2011) used a semi-analytical model of galaxy formation built on average halo growth histories (Boylan-Kolchin et al. 2010) and assumptions about typical stellar orbits to consider the accretion of metals on stars and its suppression due to stellar winds. Johnson (2015) performed a similar analysis to study the effect of radiation pressure on metal accretion and argued that radiation pressure selectively inhibits dust accretion. This implies that stars enriched by accretion from the ISM will show selective reduction in refractory elements, which may explain the composition of at least some carbon-enhanced metal-poor stars without neutron-capture element overabundance (CEMP-no stars; Beers & Christlieb 2005; Yoon et al. 2016, and references therein). By comparing the metallicities of low-mass stars with different spectral types, Hattori et al. (2014) found possible observational evidence for metal accretion on the halo and thick-disc stars of the Milky Way, and suggested that metal accretion could have occurred for the stars in the satellite galaxies before they merged into the main halo, since the velocity dispersions of these dwarf systems are much smaller than the main progenitor of the Milky Way.

Nevertheless, these studies of metal accretion by stars simplify one or both of two important aspects of the problem. First, the dynamical and chemical evolution of the ISM is often simplified, so that the density evolution (Bird et al. 2013) of gas in the Galactic disc and halo as well as its chemical evolution (Kobayashi & Nakasato 2011; Shen et al. 2012; Kulkarni et al. 2013; Shen et al. 2013, 2015) are neglected. In reality, gas density not only evolves on average as $(1 + z)^3$, but can also briefly increase accretion rates on stars during episodes of major galaxy mergers when the Galaxy has a disturbed morphology (Bird et al. 2013). Secondly, stellar orbits are also often simplified. As the Galaxy grows in mass via accretion and mergers, its potential well deepens and virial velocity increases. Major mergers can have a strong effect on stellar orbits, which can increase accretion rates for brief periods of time (Bird et al. 2013). A large fraction of stars in the bulge and halo can be formed in satellite progenitors rather than the main host halo (Pillepich, Madau & Mayer 2015). Also, before the Galaxy develops a distinct halo, stars that are in the halo today can be on radial orbits and can encounter denser-than-average gas, thus increasing the metal accretion rates. Our aim in this work is to achieve a more realistic picture for both of these ingredients of stellar metal-accretion models.

In this paper, we study the accretion of metals on halo and bulge stars using the high-resolution cosmological zoom-in simulation 'Eris' (Guedes et al. 2011). Eris creates a Milky Way analogue at $z = 0$ and represents a possible assembly history of the Galaxy. Due to its cosmological nature, Eris accounts for the cosmological inflow of metal-poor gas as well as a plausible merger history of the Galaxy. Due to its high resolution, Eris is able to evolve star particles that represent the earliest stars on realistic orbits in an evolving galactic potential. Star formation and supernova implementations lead to the chemical evolution of the ISM. These properties of Eris make it possible for us to investigate metal accretion on stars as they interact with an ISM with realistic chemical and dynamical evolution.

We describe the Eris simulation in Section 2. Section 3 details our metal-accretion model and our results are presented in Section 4. We end with a summary of our main conclusions in Section 5.

2 THE ERIS SIMULATION

We use the high-resolution, zoom-in cosmological hydrodynamical simulation 'Eris' of a Milky Way Galaxy analogue to investigate accretion of metals on to old and metal-poor stars. A detailed description of the Eris simulation is provided by Guedes et al. (2011). Here we briefly outline aspects relevant to this study. The simulation was performed with the parallel TREESPH code GASOLINE (Wadsley, Stadel & Quinn 2004) in a WMAP-3 cosmology (Spergel et al. 2007). The halo has total mass $M_{\rm vir} = 7.9 \times 10^{11}$ M$_\odot$ at $z = 0$, and was chosen to have a quiet merger history with no major merger (of mass ratio greater than 1/10) after $z = 3$. The high-resolution region, centred around a Lagrangian subregion of 1 Mpc on a side, contains 13 million dark matter particles and an equal number of gas particles, for a final dark matter and gas particle mass of $m_{\rm DM} = 9.8 \times 10^4$ M$_\odot$ and $m_{\rm SPH} = 2.0 \times 10^4$ M$_\odot$, respectively. The gravitational softening length, $\epsilon_{\rm G}$, was fixed to 120 physical pc for all particle species from $z = 9$ to the present, and evolved as $1/(1 + z)$ from $z = 9$ to the starting redshift of $z = 90$. A total number of 400 snapshots were taken. The time spacing between two subsequent snapshots is about 30 Myr.

The simulation includes a uniform metagalactic ultraviolet background (Haardt & Madau 1996), Compton cooling, atomic cooling and metallicity-dependent radiative cooling at T $<10^4$ K. Star formation is modelled by stochastically forming 'star particles' out of gas that is sufficiently cold ($T < 3 \times 10^4$ K) and reaches a threshold density of $n_{\rm SF} = 5$ atoms cm^{-3}. The local star formation rate follows:

$$\frac{{\rm d}\rho_*}{{\rm d}t} = 0.1 \frac{\rho_{\rm gas}}{t_{\rm dyn}} \propto \rho_{\rm gas}^{1.5}, \quad (1)$$

where ρ_* and $\rho_{\rm gas}$ are the stellar and gas densities, respectively, and $t_{\rm dyn}$ is the local dynamical time. Each star particle has an initial mass $m_* = 6000$ M$_\odot$ and represents a simple stellar population that follows a Kroupa, Tout & Gilmore (1993) initial mass function (IMF). Note that this IMF is also applied for the first generation of stars (Population III). In the simulation, new star particles inherit the metallicity of their parent gas particles. Star particles inject energy, mass and metals back into the ISM through Type Ia and Type II SNe, and stellar winds (Stinson et al. 2006). Eris' high resolution enables the development of an inhomogeneous ISM, which allows clustered star formation and strong cumulative feedback from coeval supernova explosions. Large-scale galactic winds are launched as a consequence of stellar feedback, which transports a substantial quantity of metals into the circumgalactic medium and enriches the subsequent gas accretion (Shen et al. 2013). At $z = 0$, Eris forms an extended, rotationally supported stellar disc with a small bulge-to-disc ratio and a radial scalelength of 2.5 kpc. The structural properties, the mass budget in various components and the scaling relations in Eris are simultaneously consistent with observations of the Galaxy (Guedes et al. 2011).

The simulation follows Raiteri, Villata & Navarro (1996) to model metal enrichment from Type Ia and Type II SNe (SN Ia and SN II). Metals are distributed to gas within the SPH smoothing kernel, which consists of 32 neighbouring particles. For SN II, metals are released as the main-sequence progenitors die, and iron and oxygen are produced according to the following fits to the Woosley & Weaver (1995) yields:

$$M_{\rm Fe} = 2.802 \times 10^{-4} \left(\frac{m_*}{{\rm M}_\odot} \right)^{1.864} {\rm M}_\odot, \quad (2)$$

and

$$M_{\rm O} = 4.586 \times 10^{-4} \left(\frac{m_*}{{\rm M}_\odot} \right)^{2.721} {\rm M}_\odot. \quad (3)$$

For SN Ia, each explosion produces 0.63 M$_\odot$ of iron and 0.13 M$_\odot$ of oxygen (Thielemann, Nomoto & Yokoi 1986). The mass return from stellar wind feedback is computed for stars with masses between 1 and 8 M$_\odot$. For each stellar particle, the amount of stars lost as supernovae during every timestep is computed following stellar lifetimes by Raiteri et al. (1996), and the returned mass is calculated using the initial–final mass relation of Weidemann (1987). The mass is distributed to neighbouring gas particles in the same way as the SNe feedback but with no energy injection. The returned gas inherits the metallicity of the star particle. We adopt the Asplund et al. (2009) solar abundance scale for the elements other than O and Fe that are not tracked in the simulation.

It is worth noting that the simulation used a traditional SPH formalism where metals advect with the fluid perfectly without mixing due to microscopic motions, and this may cause an artificially inhomogeneous chemical distribution. Following Shen et al. (2015), to model the unresolved mixing we post-process the simulation to assign each stellar particle with the *intrinsic* average metallicity of its 128 neighbouring gas particles at the formation time. The corresponding mixing length is generally around 50–120 pc at all redshifts. At our star formation threshold density of 5 atoms cm^{-3}, this corresponds to a distance that gas can cross within the free-fall time, assuming the typical velocity dispersion of a molecular cloud. We have shown in Shen et al. (2015) that, with this smoothing model, the overall chemical evolution in Eris appears to reproduce the observed [α/Fe] as a function of metallicity in the Milky Way. When we calculate the metal-accretion rate (see Section 3 for details), the gas properties are also smoothed over 128 neighbours.

3 METAL-ACCRETION MODEL

In Eris, stars are represented by collisionless star particles that are created when gas particles satisfy the temperature and density condition described in the previous section. Each star particle has an initial mass $m_* = 6000$ M$_\odot$, which reduces with time due to stellar evolution. While we cannot resolve individual stars with mass of the order of 1–100 M$_\odot$ due to unavoidable limitations imposed by numerical resolution, star particles in Eris still trace the underlying gravitational potential well. Therefore, we assume that these star particles provide a fair sample of the true stellar orbits. To calculate accretion of gas from the ISM on to stars, we assume that stars follow the orbits of star particles in Eris, and model accretion as a spherically symmetric Bondi–Hoyle flow, given by (Hoyle & Lyttleton 1939; Bondi 1952; Shima et al. 1985)

$$\dot{M} = \frac{2\pi (G M_*)^2 \rho}{\left(v_{\rm rel}^2 + c_{\rm s}^2 \right)^{3/2}}, \quad (4)$$

where M_* is the stellar mass, ρ is the gas density, $v_{\rm rel}$ is the relative velocity between the star and the gas, and $c_{\rm s}$ is the gas sound speed. For an ideal gas $c_{\rm s} = \sqrt{\gamma k_{\rm B} T / \mu m_{\rm H}}$, where γ is the adiabatic index, $k_{\rm B}$ is the Boltzmann constant, μ is the mean molecular weight and $m_{\rm H}$ is the mass of the hydrogen atom. For simplicity, we use a constant $\gamma = 5/3$ corresponding to an adiabatic gas, and a constant $\mu = 1.2$, which corresponds to primordial neutral gas. In reality, radiative cooling may reduce γ to a value between 5/3 and 1 and photoionization may decrease μ by a factor of 2. These changes to γ and μ may alter the sound speed by at most 40 per cent.

We consider gas accretion on to four classes of stars, two of which are defined by age and two by intrinsic metallicity: (1) stars formed in the first 600 Myr of the simulation and classified as halo stars at redshift $z = 0$, (2) stars formed in the first 600 Myr of the simulation and classified as bulge stars at redshift $z = 0$, (3) stars with intrinsic iron abundance as calculated in Eris [Fe/H] < -4 and classified as halo stars at redshift $z = 0$ and (4) stars with intrinsic iron abundance [Fe/H] < -4 and classified as bulge stars at redshift $z = 0$. We thus consider accretion on to two classes of halo stars and two classes of bulge stars. Stars selected by metallicity will in general have smaller ages than stars selected by our age criterion. Observed low-mass metal-poor stars lie at the intersection of the two selections. From a theoretical point of view, the two selections may be expected to bracket extreme accretion scenarios, as age-selected stars will accrete gas longer. Note that the disc, bulge and halo of the Eris Galaxy analogue at $z = 0$ are determined by kinematic decomposition as described by Guedes et al. (2011). Of all the Eris star particles falling in each group, we select a uniform random sample of 2000 star particles to compute metal accretion. Orbits of these star particles are traced to the current epoch using 400 snapshots evenly spaced in time with $\Delta t \simeq 30$ Myr. For each star particle, we compute the average gas sound speed c_s and metallicity over its 128 nearest neighbouring gas particles (Shen et al. 2015), as described in Section 2. The relative velocity v_{rel} is the velocity difference between the star particle and the centre-of-mass velocity of the neighbouring gas particles. The iron or oxygen accretion rate is then given by multiplying the averaged iron or oxygen mass fraction of the neighbouring gas by the mass accretion rate from equation (4). Fig. 1 provides a visual impression of halo and bulge stars in Eris by showing the two-dimensional probability distribution functions derived from projected stellar orbits of a uniform random sample of halo and bulge stars (orbits of only metallicity-selected stars are shown). The projection is over complete orbits so that information from all redshifts is combined.

We assume $M_* = 0.8$ M$_\odot$ while evaluating the mass accretion rate using equation (4). This approximately corresponds to the main-sequence turn-off mass in a 12-Gyr-old stellar population. The maximum stellar mass for which a star in our age-limited sample can survive up to the present day is 0.99 M$_\odot$. The lifetime of a star with mass 0.9 M$_\odot$ is 15 Gyr and that with mass 0.8 M$_\odot$ is 16.1 Gyr. Stars selected by metallicity can have much higher mass: metal-poor stars could form relatively recently in pristine pockets of the ISM that are yet to be polluted by metals; such stars can have higher mass and still survive to the present day. Still, we find that 36 per cent of the bulge star particles selected by metallicity form in the first 600 Myr of the simulation and 80 per cent form in the first Gyr. Of the halo stars selected by metallicity, 11 per cent form in the first 600 Myr and 80 per cent form in the first 1.8 Gyr. Metal mixing in the ISM is efficient enough that most metallicity-selected stars have large ages. We assume that accreted metals are mixed in surface convective zones with mass 3×10^{-3} M$_\odot$ for $M_* = 0.8$ M$_\odot$ (Yoshii 1981; Fujimoto et al. 1995). For a fixed convective zone mass fraction, the accretion rate scales as M_*^2 and the relative metal abundance ratios [X/H] scale as M_*.

4 RESULTS

With stellar orbits and gas metallicity predictions from Eris, and our metal-accretion model described in the previous section, we

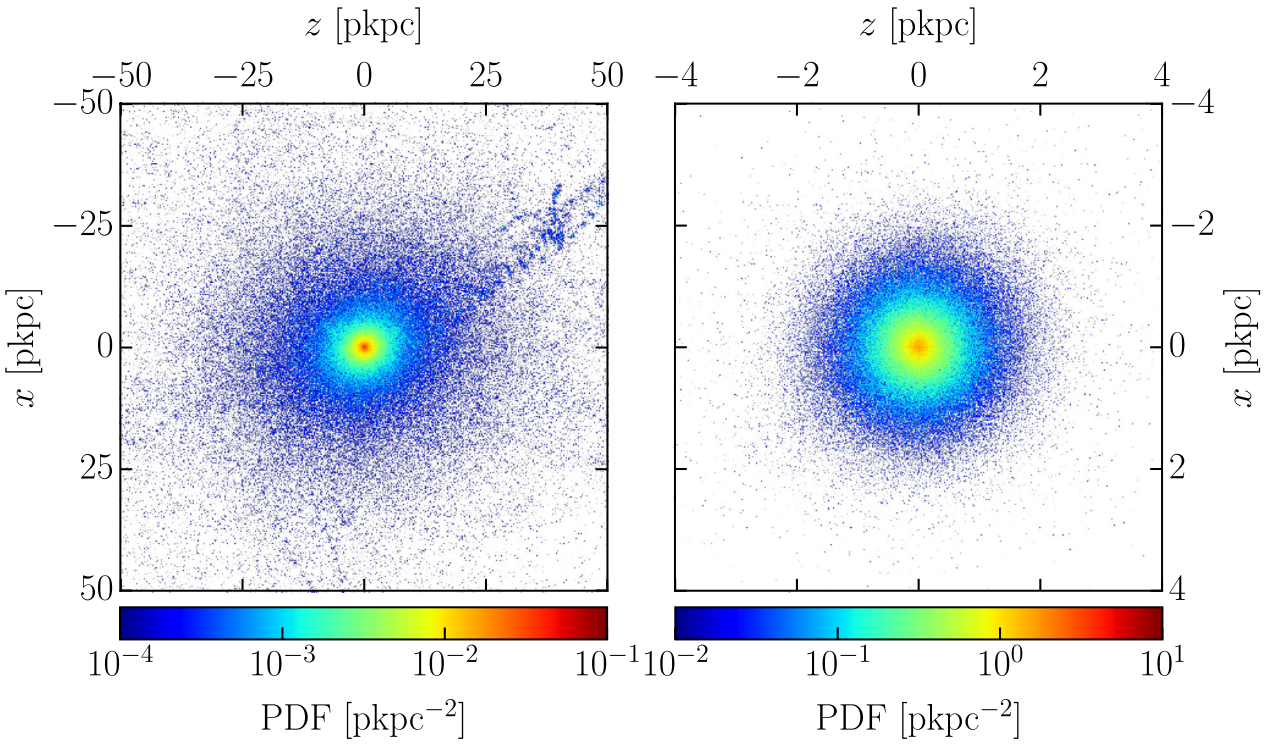

Figure 1. Two-dimensional probability distribution functions derived from projected stellar orbits in Eris for halo (left-hand panel) and bulge (right-hand panel) stars. Distances are in physical kiloparsecs (pkpc). The projection shown here is over complete stellar orbits so that information from all redshifts ($z = 0$–12) is combined. For comparison, the radial scalelength disc of the Milky Way analogue in Eris is 2.5 kpc at $z = 0$. We find that both halo and bulge stars show significantly higher incidence in the central regions of the galaxy. As a result, stars in the halo as well as the bulge are likely to encounter dense gas, which can enhance accretion.

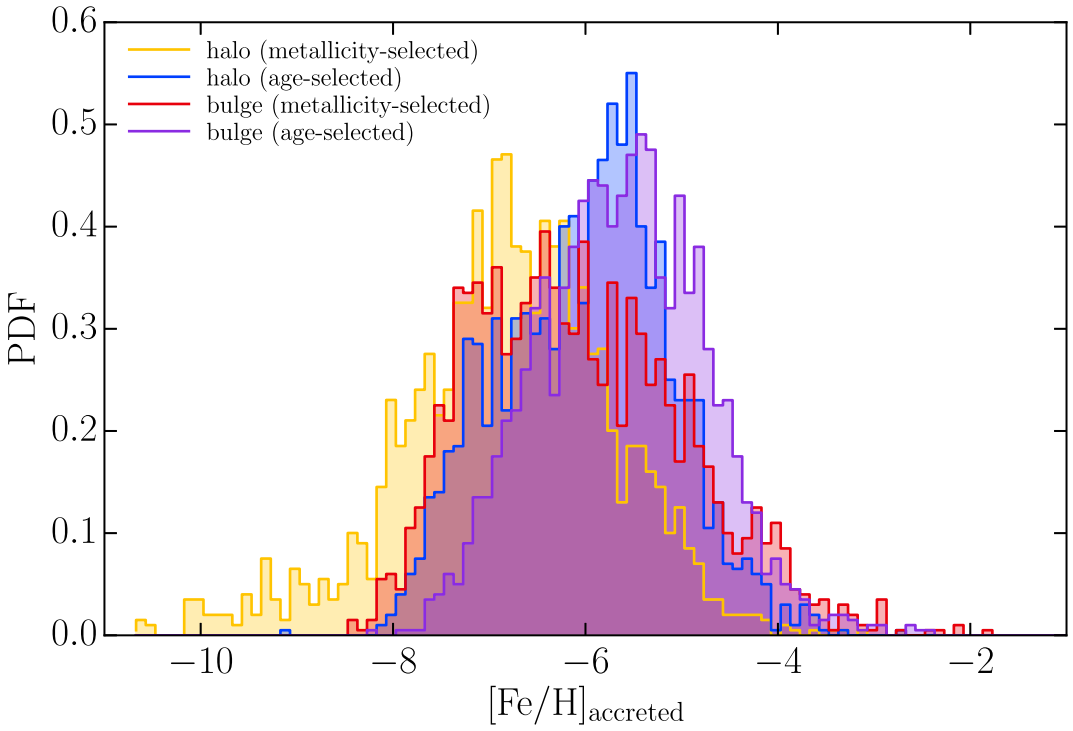

Figure 2. PDFs of accreted iron abundance [Fe/H] on to stars in our sample. Purple and red histograms show PDFs for bulge stars selected by their age and metallicity, respectively. Blue and yellow histograms show PDFs, respectively, for age- and metallicity-selected halo stars. We find that stars in our sample can be enriched up to [Fe/H] ~ -6 to -5 purely due to accretion. The spread in these PDFs is due to the distribution of stellar orbits and gas metallicities in the galaxy. As a reference, the minimum observable iron abundance is about [Fe/H] $= -9.8$ (Frebel & Norris 2013).

can now consider metal enrichment of halo and bulge stars due to accretion.

4.1 Metal accretion in Eris

Fig. 2 shows probability distribution functions (PDFs) of the relative abundance values [Fe/H] of accreted iron for the four categories of stars defined in Section 3. The four PDFs are quite similar, perhaps surprisingly so. They peak around [Fe/H] ~ -6 to -5, well within the metallicity detection limit of modern surveys (Frebel & Norris 2013) and comparable to the metallicities of the most metal-poor stars known (Caffau et al. 2011; Keller et al. 2014). This indicates that accretion can have a significant impact on metal-poor main-sequence stars. The four PDFs also show a considerable scatter – about three decades around their average values. The remarkable agreement between the four distributions results from the fact that both halo and bulge stars encounter dense gas in the central regions of the galaxy. This is evident in Fig. 1, which shows that both halo and bulge stars exhibit a significantly higher incidence in the central regions. This is understandable, as a kinematically distinct halo and bulge do not exist in Eris at redshift $z > 2$, and the last major merger of the galaxy is at $z \sim 3$. Additionally, the [Fe/H] PDFs of age- and metallicity-selected samples also agree quite well, because most metallicity-selected stars ([Fe/H] < -4) are quite old. As mentioned above, 80 per cent of metallicity-selected halo stars were formed within the first 1.8 Gyr of the simulation, while the same fraction of metallicity-selected bulge stars were formed within the first 1 Gyr. Thus, regardless of how they are selected at redshift $z = 0$, halo as well as bulge stars in our analysis accrete to a level of [Fe/H] ~ -6 to -5 on average.

While the four distributions in Fig. 2 are remarkably similar, there are small differences. Age-selected bulge stars have the highest median accretion ([Fe/H] $= -4.9$ with a 68 per cent spread of 1.7), followed by age-selected halo stars ([Fe/H] $= -5.2$ with a 68 per cent spread of 1.8), and metallicity-selected bulge stars ([Fe/H] $= -5.4$ with a 68 per cent spread of 2.3). Metallicity-selected halo stars have the lowest value, [Fe/H] $= -6.0$ with a 68 per cent spread of 2.0. The age-selected sample of bulge stars has the highest accreted metallicity, while the metallicity-selected sample of halo stars shows the lowest accreted metallicity. The PDFs of age-selected halo stars and metallicity-selected bulge stars have intermediate values. This difference is still quite small compared to the overall spread of the PDFs. This ordering of the PDFs can also be understood from the small differences in ages and orbital distribution of stars in the four samples. Age-selected stars in our analysis are marginally older than the metallicity-selected stars and therefore on an average accrete metals for a longer duration, resulting in higher [Fe/H]. Likewise, bulge stars encounter marginally denser gas than halo stars, as seen in Fig. 1, which boosts the accretion rates on to bulge stars. Our finding that metal-poor bulge stars are generally older than metal-poor halo stars is along the lines of previous theoretical results (White & Springel 2000; Brook et al. 2007; Tumlinson 2010). This explains the ordering of the histograms for metallicity-selected samples in Fig. 2.

The result in Fig. 2 describes accretion on to 0.8 $M_\odot$ main-sequence stars, but it is possible to understand how it will change for different stellar masses. For a fixed convective-zone mass fraction, the accreted metal abundance [Fe/H] scales with M_*. For smaller stellar masses, the enrichment levels will drop due to the reduced accretion rate and enhanced convective layer mass. For a 0.6 $M_\odot$

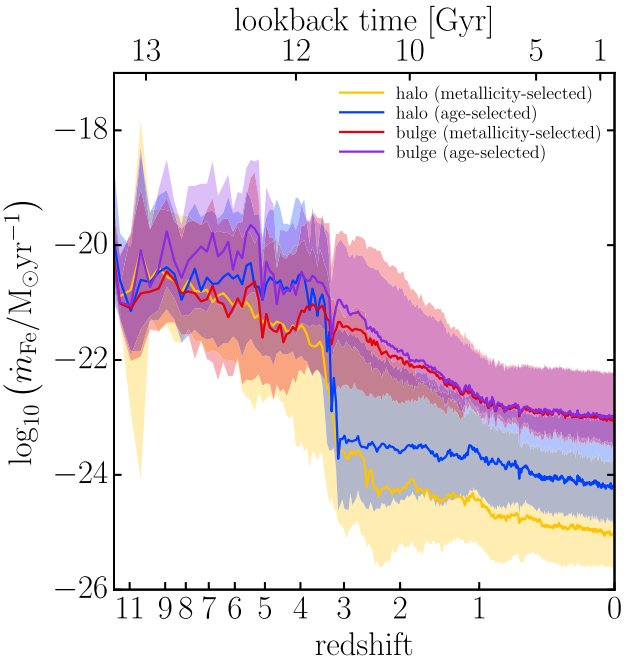

Figure 3. Evolution of the metal-accretion rate in our four samples of stars. Solid curves show the median values and shaded regions show 68 per cent scatter around the median. Blue and yellow curves and shaded regions describe properties of halo stars selected by age and metallicity, respectively. Bulge stars selected by age and metallicity are described, respectively, by purple and red curves. The sudden drop in the accretion rates on to halo stars at $z \sim 3.1$ is associated with the last major merger of the galaxy.

main-sequence star, the convective zone mass increases to $\sim 10^{-2}$ $M_\odot$ (Yoshii 1981) while the accretion rate drops by a factor of 1.8. As a result, the histograms in Fig. 2 will shift towards lower values of [Fe/H] by about two decades. Old stars with masses greater than 0.8 $M_\odot$ will likely be on the giant branch today. Although accretion rates of these stars remain quite high, the resultant [Fe/H] ratios drop because of larger convective zone masses, which are of the order of 10^{-1} $M_\odot$ for giants (Yoshii 1981). In this case the histograms in Fig. 2 will shift towards lower values of [Fe/H] by almost three decades. Fig. 2 thus presents as extreme case. Negative feedback from processes such as stellar winds and radiation feedback may also reduce accretion (Johnson & Khochfar 2011; Johnson 2015). Our results from Fig. 2 predict marginally higher accreted metallicity than the model of Frebel et al. (2009). Our results are closer to the extreme model of Frebel et al. (2009), in which it is assumed that the stars pass once through a dense cloud with density $n \sim 10^3$ cm^{-3}. This difference is mainly because the gas density increases quite rapidly towards high redshift, while Frebel et al. (2009) only consider accretion from a static gas disc with height 100 pc and density $n \sim 5$ cm^{-3}. The median accreted [Fe/H] in their fiducial model is about -7. This increases to -5 in their extreme model. The latter value is closer to the median values of all four samples of stars in Fig. 2. Our median values are in agreement with predictions by Komiya et al. (2015) obtained from a semi-analytical galaxy formation model built on halo merger trees.

4.2 Understanding metal-accretion rates

In order to understand the stellar metal-accretion levels in our model, Figs 3 and 4 show the evolution of various relevant quantities in Eris for the four samples of stars considered. Fig. 3 shows the evolution of the metal-accretion rate of iron. Yellow and blue curves correspond to the metallicity- and age-selected samples, respectively, of halo stars. Red and purple curves correspond to bulge stars. Solid curves show the evolution of the median value; shaded regions in corresponding colours show ranges of 68 per cent scatter around the medians. We see that the average metal-accretion rate increases as we go towards higher redshifts. All four categories of stars have very similar accretion rates at redshifts $z > 3$. It is only at lower redshifts ($z < 3$), after the last major merger of the Eris Milky Way, that halo and bulge stars kinematically separate with halo stars occupying regions with low gas density and therefore low accretion rates. The average metal accretion rate at high redshifts is about 10^{-20} $M_\odot$ yr^{-1}. By $z = 0$, this drops by two orders of magnitude for bulge stars and by four orders of magnitude for halo stars. Note that the difference between the metal-accretion rates of age- and metallicity-selected stars is relatively small. This is simply because our metallicity-selected samples are also predominantly composed of old stars, as explained above.

The relatively high values of accretion rates at high redshift are driven by the gas density evolution. This is evident in panel (a) of Fig. 4, which shows the evolution of the average physical density of gas along the stellar orbits in each of our four samples. The difference between the four curves is along the lines of what we expect – metallicity-selected halo stars encounter the lowest gas density, while the age-selected bulge stars encounter the highest gas density. This difference explains the trends in the accretion rates shown in Fig. 3 as well as in the histograms of accreted [Fe/H] in Fig. 2. The black curve in panel (a) shows the evolution of the average density within the virial radius of the halo. The virial density evolves at $(1 + z)^3$. A comparison between the virial density curve and the median gas density curves shows that the density of gas encountered by stars in our samples grows roughly as $(1 + z)^3$ from redshift $z = 0$ to 6, and then drops because the halo turns around. Importantly, the stars in our samples encounter a significantly higher gas density than the virial density as both halo and bulge stars are centrally concentrated compared to the virial radius, as in Fig. 1. This can be understood further with help from the brown dot–dashed, dashed and solid curves in panel (a) of Fig. 4. These curves show the average gas density in Eris within 25, 2 and 0.5 physical kpc (pkpc), respectively. At high redshifts, $z > 3$, almost all stars in all four of our samples are interacting with gas within in the inner 2 pkpc of the progenitor haloes of the Milky Way. This gas density is considerably higher than the gas density assumed in previous works (cf. Frebel et al. 2009; Johnson & Khochfar 2011), which results in the high metal accretion seen in Fig. 2. This picture is reinforced by panel (b) of Fig. 4, which shows the evolution of the radial distribution of the stars in our four samples. The solid curves in this panel show the radial distance of stars from centres of mass of respective host haloes with the scatter represented by the shaded areas. All four samples of stars are quite centrally concentrated. The halo stars generally have larger radial separations than the bulge stars, which explains the density trends seen in panel (a).

In panel (c), Fig. 4 shows the evolution of the relative velocity of stars with respect to ambient gas. The velocity decreases with increasing redshift due to the decreasing halo mass. This also increases the accretion rate. While accretion rates at high redshift are enhanced by increased gas density and reduced velocities, the gas metallicity evolution restricts the enhancement. The brown dashed curve in this panel shows the evolution of the circular velocity $v_{\rm circ}$ at the virial radius, while the black dashed curve shows the evolution of the maximum rotational velocity $v_{\rm max}$ in the main progenitor halo of the Eris galaxy. Stars in all four samples tend to have lower

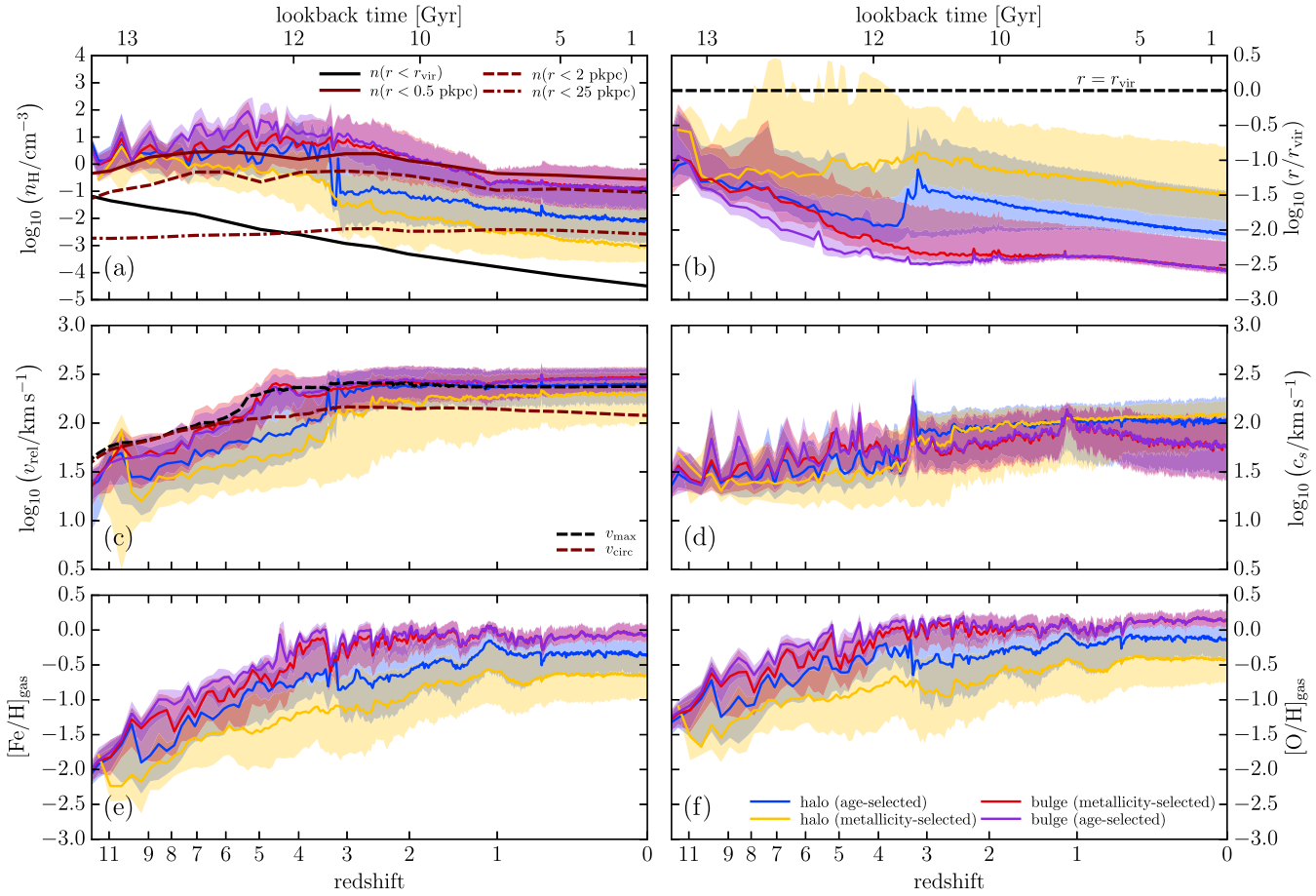

Figure 4. Evolution of various quantities in Eris: (a) gas density; (b) radial distance of stars from centres of mass of respective host haloes; (c) stellar relative velocity with respect to the gas; (d) gas sound speed; (e) gas–iron abundance [Fe/H]; (e) gas–oxygen abundance [O/H]. Gas densities, sound speed and metal abundances refer to gas along stellar orbits. In each panel, solid curves show median quantities and shaded regions show 68 per cent scatter around the median. Blue and yellow curves and shaded regions describe properties of halo stars selected by age and metallicity, respectively. Bulge stars selected by age and metallicity are described, respectively, by purple and red curves. In panel (a), the black curve shows the average gas density within the virial radius. Brown dot–dashed, dashed and solid curves in this panel show the evolution of density averaged within 25, 2 and 0.5 pkpc from the centres of mass of progenitor haloes of the Eris Milky Way. In panel (c), the brown dashed curve shows the evolution of the circular velocity $v_{\rm circ}$ at the virial radius. The black dashed curve in this panel shows the evolution of the maximum rotational velocity $v_{\rm max}$. Densities and velocities are in physical units.

velocity than $v_{\rm max}$, as the rotation curve drops at small radii. The stellar velocities can also be compared with the evolution of the gas sound speed, which is shown in panel (d). The sound speed decreases towards higher redshift with reduced gas temperature. Panels (e) and (f) of Fig. 4 show the evolution of the iron and oxygen abundances of the gas along orbits of stars in our four samples. There is a metallicity gradient in the ISM with most metal-enriched gas present near the centre of the halo. This metallicity gradient is also seen in other simulations of the Galaxy's assembly (e.g. Stinson et al. 2013). As a result, bulge stars accrete relatively more metal-rich gas compared to halo stars. The metallicity of gas around bulge stars evolves from [Fe/H] $= -1.5$ at $z \sim 10$ to [Fe/H] $= 0.0$ at $z = 0$. The oxygen abundance evolves from [O/H] $= -1.0$ to [O/H] $= 0.1$ in this redshift range. The metallicity of gas around halo stars is lower by about 0.7. The resultant α-enhancement of ISM gas at high redshift by about 0.5 relative to low redshifts is seen in panel (e) of Fig. 4, which shows the evolution of [O/Fe].

Fig. 5 shows the resultant [O/Fe] ratio at $z = 0$ due to accretion in the four classes of stars considered here, as a function of the accreted [Fe/H]. This α-enhancement is shown in comparison with observed [α/Fe] ratios from disc and halo stars in the Galaxy (Fulbright 2000; Reddy et al. 2003; Cayrel et al. 2004; Simmerer et al. 2004; Venn et al. 2004; Barklem et al. 2005; Reddy, Lambert & Allende Prieto 2006; Mishenina et al. 2013; Roederer et al. 2014). The accreted [O/Fe] ratios are in agreement with the [O/Fe] ratios seen in the most metal-poor stars (see also Puzia, Kissler-Patig & Goudfrooij 2006). At iron abundances of [Fe/H] > -1 the observed [O/Fe] drops sharply to less than $\sim$0.2, signalling the effect of SN Ia (Tinsley 1979). The accreted α-enhancements are much higher. The reason is clear from Fig. 3 – stars in all four of our samples accrete most of their metals at high redshifts before SN Ia start playing an important role. Thus, most accreted gas is α-enhanced (cf. panels (e) and (f) of Fig. 4). This also tells us that measurements of [α/Fe] will not help in separating stars with intrinsic metal enrichment from stars that have accreted their metals. Perhaps the only way to disentangle these stars would be to observe a peculiar enrichment pattern that is unlikely to exist in the low-redshift ISM, such as the enhanced [Si/C] ratio or the large contrast between the abundances of odd and even element pairs that is predicted for pair-instability supernovae (Heger & Woosley 2002; Aoki et al. 2014).

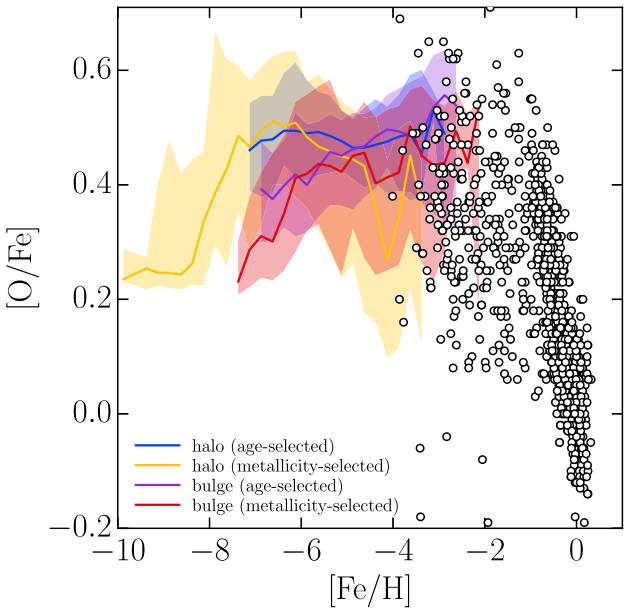

Figure 5. Median α-enhancement [O/Fe] of accreted gas by stars in the four samples considered in this paper (solid curves) and 68 per cent scatter around the median (shaded regions). Blue and yellow curves and shaded regions describe properties of halo stars selected by age and metallicity, respectively. Bulge stars selected by age and metallicity are described, respectively, by purple and red curves. Open circles show [α/Fe] measurements for halo and disc stars from the compilation by Shen et al. (2015). There is a good agreement between the [α/Fe] for iron-poor stars and the accreted gas in our model.

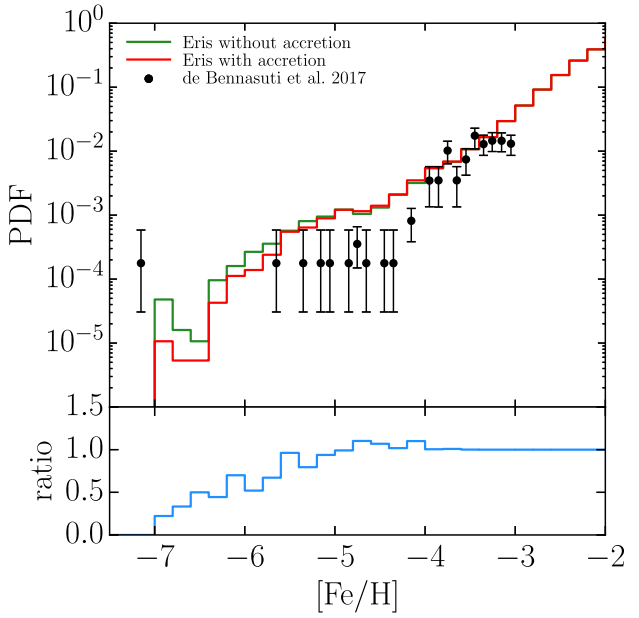

Figure 6. The MDF of halo stars in Eris simulation with (red curve) and without (green curve) accounting for metal accretion by stars from the ISM. The data points from the compilation by de Bennassuti et al. (2017). The blue curve in the lower panel shows the ratio of the two MDFs, illustrating the truncation of the low-metallicity tail of the MDF due to accretion.

4.3 Effect of accretion on the MDF

Most models of Galactic chemical enrichment – including our base Eris simulation – assume that enrichment of stars due to accretion of gas from the ISM is negligible. In Fig. 6, we consider the error incurred due to this assumption. Black symbols in this figure show the measured metallicity distribution function (MDF) as compiled by de Bennassuti et al. (2017), shown here as a PDF. The green histogram shows the MDF of halo stars from Eris without any correction due to accretion. This histogram refers to the intrinsic metallicity of halo stars in Eris. The red histogram in Fig. 6 shows how the black histogram is modified when accretion is taken into account. In each [Fe/H] bin, stars are added from lower metallicity bins by gaining excess [Fe/H] due to accretion, in proportion to the PDF derived in Fig. 2. Similarly, each [Fe/H] bin loses stars to higher metallicity bins due to accretion. Only the metallicity-selected sample of halo stars (which has stars that have [Fe/H] < -4 at $z = 0$) is used for this purpose. The predicted MDFs agree quite well with observations.

As described in previous sections, enrichment due to accretion is small ([Fe/H] ~ -6 to -5 on average). Therefore, accretion affects only the metal-poor tail of the MDF; the MDF at high metallicities remains unmodified. However, the effect on the MDF at [Fe/H] < -5 is considerable, suggesting that a large fraction of metal-poor stars in this regime could be potentially enriched due to accretion. This is emphasized by the bottom panel of Fig. 6, which shows the ratios of the uncorrected and corrected MDFs from the top panel. Accretion truncates the low-metallicity end of the MDFs to about [Fe/H] $= -7$. Metal abundance measurements of these stars would then contain little or no information about the chemistry of their natal environments, thus affecting any inference of the Population III IMF from these stars (e.g. Salvadori et al. 2007; Schneider et al. 2012; Hartwig et al. 2015; de Bennassuti et al. 2017). It should also be noted that accretion may change the relative abundances of elements by a greater degree than the absolute abundance of a single element. Johnson (2015) has proposed that if stars do indeed accrete metals from the ISM, then radiation pressure would selectively inhibit accretion of dust grains. As a result, if most metal enrichment in these stars is due to accretion, then refractory elements such as iron would appear to be selectively depleted. This pattern of metal enrichment is tantalizingly similar to that seen in carbon-enhanced metal poor (CEMP) stars (Beers & Christlieb 2005; Yoon et al. 2016, and references therein). Seven of the eight stars with [Fe/H] < -4.5 are carbon-enhanced. The one star with low-carbon abundance (Caffau et al. 2011) could still be a CEMP star with a carbon abundance that is yet to be detected, possibly because of the limited spectral signal-to-noise ratio (S/N) and warm temperature.[1] The argument of Johnson (2015) would then suggest that the known metal-poor stars have been enriched mostly by accretion of metals from the ISM. This is in good agreement with what we find in Fig. 6.

5 CONCLUSIONS

We have studied the chemical enrichment of stars due to accretion of metal-enriched gas from the ISM during the Milky Way's development, using the Eris zoom-in cosmological simulation of assembly of a Milky Way analogue. We considered metal-poor and old stars in both the Galactic halo and bulge and make use of the stellar orbits and gas density and metallicity distributions predicted by Eris.

[1] This is the case, for instance, for the Group II CEMP-no stars G64-12 and G64-37, which were not recognized as CEMP until extremely high S/N spectra were obtained (Placco et al. 2016).

Our main conclusion is that both halo and bulge stars accrete metals from the ISM and, in extreme cases, can reach enrichment levels of [Fe/H] ~ -2 due to accretion alone. The median enrichment level is about [Fe/H] ~ -6 to -5 for age- as well as metallicity-selected stars in both the halo and bulge. There is little difference in the accreted enrichment levels of the four classes of stars, although metallicity-selected halo stars tend to accrete the least amount of metals. Metal-poor bulge stars are generally older than metal-poor halo stars. As a result, bulge stars show a marginally higher degree of effect of accretion. Halo and bulge stars accrete metals at the rate of about 10^{-24} and 10^{-22} $M_\odot$ yr^{-1}, respectively, at redshifts $z \lesssim 3$, but this accretion rate increases a hundred-fold to about 10^{-20} $M_\odot$ yr^{-1} at higher redshifts due to increased gas density. The drop in accretion rates with time is mainly because of decreasing gas density. Bulge and halo stars accrete similar amounts of metals at high redshifts as kinematically distinct bulge and halo are not yet developed at these redshifts and both sets of stars encounter similar metal distribution in the ISM on average.

Because accretion mostly takes place at high redshifts, it is α-enriched to [α/Fe] ~ 0.5. This is comparable to the α-enrichment levels seen in the most metal-poor stars. It also means that α-enrichment does not act as a discriminant between intrinsically and extrinsically enriched stars. Accretive metal enrichment is sufficient to change the predicted MDF of halo stars at [Fe/H] < -5. This suggests that attempts to infer the natal chemical environment of the most metal-poor stars from their observed enrichment today can be hindered due to metal accretion. Our analysis assumes a stellar mass of 0.8 $M_\odot$. Accreted metal enrichment level drops rapidly at smaller stellar masses due to decreasing accretion rates and increased convective zone masses. This faint dwarfs will be more likely to probe the first generation of stars. Peculiar enrichment patterns such as those predicted to arise from pair-instability supernovae could help in disentangling natal and accreted metal content of stars (Aoki et al. 2014). Most stars are rich in oxygen and carbon with [O/H] < -3.2 and [C/H] < -3.5. The accreted gas in our model only has [O/Fe] $= 0.5$. Therefore, although the iron abundance is significantly enhanced by accretion, the abundance in elements such as C and O should still remain unchanged and could be useful in probing Population III. Also, our findings suggest that lowest-metallicity Damped Lyman-α Systems (Erni et al. 2006; Cooke, Pettini & Murphy 2012; Salvadori & Ferrara 2012; Kulkarni et al. 2013) would provide an important cross-check for Population III yields inferred from metal-poor stars.

ACKNOWLEDGEMENTS

We thank the referee, Timothy Beers, for his positive comments and constructive suggestions, and also acknowledge helpful discussions with Andrew Casey, Ryan Cooke, Denis Erkal, Gerry Gilmore, Martin Haehnelt, Kohei Hattori, Joseph Hennawi, Sergey Koposov, Thomas Masseron, Max Pettini, Enrico Ramirez-Ruiz, Alberto Rorai and Stefania Salvadori. SS gratefully acknowledges support by Science and Technology Facilities Council and by European Research Council (ERC) Starting Grant 638707 'Black holes and their host galaxies: coevolution across cosmic time'. GK and SS acknowledge support from ERC Advanced Grant 320596 'The Emergence of Structure During the Epoch of Reionization'. Support for this work was provided by National Aeronautics and Space Administration (NASA) through grant HST-AR-13904.001-A (PM). PM also acknowledges a NASA contract supporting the Wide-Field Infrared Survey Telescope-Extragalactic Potential Observations (WFIRST-EXPO) Science Investigation Team (15-WFIRST15-0004), administered by Goddard Space Flight Center, and thanks the Préfecture of the Ile-de-France Region for the award of a Blaise Pascal International Research Chair, managed by the Fondation de l'Ecole Normale Supérieure. This work used the Distributed research utilising Advanced Computing (DiRAC)/Darwin Supercomputer hosted by the University of Cambridge High Performance Computing Service (http://www.hpc.cam.ac.uk/), provided by Dell Inc. using Strategic Research Infrastructure Funding from the Higher Education Funding Council for England and funding from the Science and Technology Facilities Council.

REFERENCES

Alcock C., Illarionov A., 1980, ApJ, 235, 541
Aoki W., Tominaga N., Beers T. C., Honda S., Lee Y. S., 2014, Science, 345, 912
Asplund M., Grevesse N., Sauval A. J., Scott P., 2009, ARA&A, 47, 481
Barkana R., Loeb A., 2001, Phys. Rep., 349, 125
Barklem P. S. et al., 2005, A&A, 439, 129
Beers T. C., Christlieb N., 2005, ARA&A, 43, 531
Beers T. C., Preston G. W., Shectman S. A., 1985, AJ, 90, 2089
Beers T. C., Preston G. W., Shectman S. A., 1992, AJ, 103, 1987
Bird J. C., Kazantzidis S., Weinberg D. H., Guedes J., Callegari S., Mayer L., Madau P., 2013, ApJ, 773, 43
Bond H. E., 1981, ApJ, 248, 606
Bondi H., 1952, MNRAS, 112, 195
Boylan-Kolchin M., Springel V., White S. D. M., Jenkins A., 2010, MNRAS, 406, 896
Bromm V., 2013, Rep. Prog. Phys., 76, 112901
Bromm V., Larson R. B., 2004, ARA&A, 42, 79
Bromm V., Yoshida N., Hernquist L., McKee C. F., 2009, Nature, 459, 49
Brook C. B., Kawata D., Scannapieco E., Martel H., Gibson B. K., 2007, ApJ, 661, 10
Caffau E. et al., 2011, Nature, 477, 67
Carney B. W., Laird J. B., Latham D. W., Aguilar L. A., 1996, AJ, 112, 668
Casey A. R., Schlaufman K. C., 2015, ApJ, 809, 110
Cayrel R. et al., 2004, A&A, 416, 1117
Christlieb N., 2003, in Schielicke R. E., ed., Reviews in Modern Astronomy Vol. 16, The Cosmic Circuit of Matter. Wiley, New York, p. 191
Ciardi B., Ferrara A., 2005, Space Sci. Rev., 116, 625
Clark P. C., Glover S. C. O., Klessen R. S., Bromm V., 2011, ApJ, 727, 110
Cooke R., Pettini M., Murphy M. T., 2012, MNRAS, 425, 347
de Bennassuti M., Schneider R., Valiante R., Salvadori S., 2014, MNRAS, 445, 3039
de Bennassuti M., Salvadori S., Schneider R., Valiante R., Omukai K., 2017, MNRAS, 465, 926
Dopcke G., Glover S. C. O., Clark P. C., Klessen R. S., 2013, ApJ, 766, 103
Erb D. K., Shapley A. E., Pettini M., Steidel C. C., Reddy N. A., Adelberger K. L., 2006, ApJ, 644, 813
Erni P., Richter P., Ledoux C., Petitjean P., 2006, A&A, 451, 19
Frebel A., Norris J. E., 2013, in Oswalt T. D., Gilmore G., eds, Planets, Stars and Stellar Systems Vol. 5. Springer Science+Business Media, Dordrecht, p. 55
Frebel A., Norris J. E., 2015, ARA&A, 53, 631
Frebel A., Johnson J. L., Bromm V., 2009, MNRAS, 392, L50
Fujimoto M. Y., Sugiyama K., Iben I., Jr, Hollowell D., 1995, ApJ, 444, 175
Fulbright J. P., 2000, AJ, 120, 1841
Glover S., 2005, Space Sci. Rev., 117, 445
Greif T. H., Springel V., White S. D. M., Glover S. C. O., Clark P. C., Smith R. J., Klessen R. S., Bromm V., 2011, ApJ, 737, 75
Griffen B. F., Dooley G. A., Ji A. P., O'Shea B. W., Gómez F. A., Frebel A., 2016, MNRAS, preprint (arXiv:1611.00759)
Guedes J., Callegari S., Madau P., Mayer L., 2011, ApJ, 742, 76
Haardt F., Madau P., 1996, ApJ, 461, 20
Hartwig T., Bromm V., Klessen R. S., Glover S. C. O., 2015, MNRAS, 447, 3892

Hattori K., Yoshii Y., Beers T. C., Carollo D., Lee Y. S., 2014, ApJ, 784, 153
Heger A., Woosley S. E., 2002, ApJ, 567, 532
Hirano S., Hosokawa T., Yoshida N., Umeda H., Omukai K., Chiaki G., Yorke H. W., 2014, ApJ, 781, 60
Howes L. M. et al., 2015, Nature, 527, 484
Howes L. M. et al., 2016, MNRAS, 460, 884
Hoyle F., Lyttleton R. A., 1939, Proc. Camb. Phil. Soc., 35, 405
Iben I., Jr, 1983, Mem. Soc. Astron. Ital., 54, 321
Ishiyama T., Sudo K., Yokoi S., Hasegawa K., Tominaga N., Susa H., 2016, ApJ, 826, 9
Jacobson H. R. et al., 2015, ApJ, 807, 171
Johnson J. L., 2015, MNRAS, 453, 2771
Johnson J. L., Khochfar S., 2011, MNRAS, 413, 1184
Keller S. C. et al., 2014, Nature, 506, 463
Kobayashi C., Nakasato N., 2011, ApJ, 729, 16
Komiya Y., Habe A., Suda T., Fujimoto M. Y., 2009, ApJ, 696, L79
Komiya Y., Habe A., Suda T., Fujimoto M. Y., 2010, ApJ, 717, 542
Komiya Y., Suda T., Fujimoto M. Y., 2015, ApJ, 808, L47
Kroupa P., Tout C. A., Gilmore G., 1993, MNRAS, 262, 545
Kulkarni G., Rollinde E., Hennawi J. F., Vangioni E., 2013, ApJ, 772, 93
Machida M. N., Nakamura T., 2015, MNRAS, 448, 1405
Maeder A., Meynet G., 1989, A&A, 210, 155
Maiolino R. et al., 2008, A&A, 488, 463
Marassi S., Chiaki G., Schneider R., Limongi M., Omukai K., Nozawa T., Chieffi A., Yoshida N., 2014, ApJ, 794, 100
Mishenina T. V., Pignatari M., Korotin S. A., Soubiran C., Charbonnel C., Thielemann F.-K., Gorbaneva T. I., Basak N. Y., 2013, A&A, 552, A128
Ness M., Freeman K., 2016, Publ. Astron. Soc. Aust., 33, e022
Norris J. E., Christlieb N., Korn A. J., Eriksson K., Bessell M. S., Beers T. C., Wisotzki L., Reimers D., 2007, ApJ, 670, 774
Pillepich A., Madau P., Mayer L., 2015, ApJ, 799, 184
Placco V. M., Beers T. C., Reggiani H., Meléndez J., 2016, ApJ, 829, L24
Puzia T. H., Kissler-Patig M., Goudfrooij P., 2006, ApJ, 648, 383
Rafelski M., Wolfe A. M., Prochaska J. X., Neeleman M., Mendez A. J., 2012, ApJ, 755, 89
Raiteri C. M., Villata M., Navarro J. F., 1996, A&A, 315, 105
Reddy B. E., Tomkin J., Lambert D. L., Allende Prieto C., 2003, MNRAS, 340, 304
Reddy B. E., Lambert D. L., Allende Prieto C., 2006, MNRAS, 367, 1329
Ripamonti E., Abel T., 2006, in Haardt F., Gorini V., Moschella U., Colpi M., eds, Joint Evolution of Black Holes and Galaxies. Taylor & Francis Group, Boca Raton, FL, p. 239
Roederer I. U., Preston G. W., Thompson I. B., Shectman S. A., Sneden C., Burley G. S., Kelson D. D., 2014, AJ, 147, 136
Ryan S. G., Norris J. E., 1991, AJ, 101, 1865
Salvadori S., Ferrara A., 2012, MNRAS, 421, L29
Salvadori S., Schneider R., Ferrara A., 2007, MNRAS, 381, 647
Schneider R., Salvaterra R., Ferrara A., Ciardi B., 2006, MNRAS, 369, 825
Schneider R., Omukai K., Limongi M., Ferrara A., Salvaterra R., Chieffi A., Bianchi S., 2012, MNRAS, 423, L60
Shen S., Madau P., Aguirre A., Guedes J., Mayer L., Wadsley J., 2012, ApJ, 760, 50
Shen S., Madau P., Guedes J., Mayer L., Prochaska J. X., Wadsley J., 2013, ApJ, 765, 89
Shen S., Cooke R. J., Ramirez-Ruiz E., Madau P., Mayer L., Guedes J., 2015, ApJ, 807, 115
Shima E., Matsuda T., Takeda H., Sawada K., 1985, MNRAS, 217, 367
Simmerer J., Sneden C., Cowan J. J., Collier J., Woolf V. M., Lawler J. E., 2004, ApJ, 617, 1091
Smith B. D., Wise J. H., O'Shea B. W., Norman M. L., Khochfar S., 2015, MNRAS, 452, 2822
Spergel D. N. et al., 2007, ApJS, 170, 377
Stacy A., Bromm V., 2014, ApJ, 785, 73
Stacy A., Bromm V., Lee A. T., 2016, MNRAS, 462, 1307
Stinson G., Seth A., Katz N., Wadsley J., Governato F., Quinn T., 2006, MNRAS, 373, 1074
Stinson G. S. et al., 2013, MNRAS, 436, 625
Susa H., Hasegawa K., Tominaga N., 2014, ApJ, 792, 32
Talbot R. J., Jr, Newman M. J., 1977, ApJS, 34, 295
Thielemann F.-K., Nomoto K., Yokoi K., 1986, A&A, 158, 17
Tinsley B. M., 1979, ApJ, 229, 1046
Tumlinson J., 2010, ApJ, 708, 1398
Venn K. A., Irwin M., Shetrone M. D., Tout C. A., Hill V., Tolstoy E., 2004, AJ, 128, 1177
Wadsley J. W., Stadel J., Quinn T., 2004, New A, 9, 137
Weidemann V., 1987, A&A, 188, 74
White S. D. M., Springel V., 2000, in Weiss A., Abel T. G., Hill V., eds, The First Stars. Springer-Verlag, Berlin, p. 327
Woosley S. E., Weaver T. A., 1995, ApJS, 101, 181
Yanny B. et al., 2009, AJ, 137, 4377
Yoon J. et al., 2016, ApJ, 833, 20
Yoshii Y., 1981, A&A, 97, 280

This paper has been typeset from a TEX/LATEX file prepared by the author.